ORIGINAL PAPER

Check for
updates

Long wave generation and coastal amplification due to propagating atmospheric pressure disturbances

Gozde Guney Dogan, et al. *[full author details at the end of the article]*

Abstract

Meteotsunamis are long waves generated by displacement of a water body due to atmospheric pressure disturbances that have similar spatial and temporal characteristics to landslide tsunamis. NAMI DANCE that solves the nonlinear shallow water equations is a widely used numerical model to simulate tsunami waves generated by seismic origin. Several validation studies showed that it is highly capable of representing the generation, propagation and nearshore amplification processes of tsunami waves, including inundation at complex topography and basin resonance. The new module of NAMI DANCE that uses the atmospheric pressure and wind forcing as the other inputs to simulate meteotsunami events is developed. In this paper, the analytical solution for the generation of ocean waves due to the propagating atmospheric pressure disturbance is obtained. The new version of the code called NAMI DANCE SUITE is validated by comparing its results with those from analytical solutions on the flat bathymetry. It is also shown that the governing equations for long wave generation by atmospheric pressure disturbances in narrow bays and channels can be written similar to the 1D case studied for tsunami generation and how it is integrated into the numerical model. The analytical solution of the linear shallow water model is defined, and results are compared with numerical solutions. A rectangular shaped flat bathymetry is used as the test domain to model the generation and propagation of ocean waves and the development of Proudman resonance due to moving atmospheric pressure disturbances. The simulation results with different ratios of pressure speed to ocean wave speed (Froude numbers) considering sub-critical, critical and super-critical conditions are presented. Fairly well agreements between analytical solutions and numerical solutions are obtained. Additionally, basins with triangular (lateral) and stepwise shelf (longitudinal) cross sections on different slopes are tested. The amplitudes of generated waves at different time steps in each simulation are presented with discussions considering the channel characteristics. These simulations present the capability of NAMI DANCE SUITE to model the effects of bathymetric conditions such as shelf slope and local bathymetry on wave amplification due to moving atmospheric pressure disturbances.

Keywords Meteotsunami · Atmospheric pressure disturbance · Atmospheric forcing · Long wave · Numerical modeling · Amplification · Proudman resonance · NAMI DANCE

1 Introduction

Tsunamis are the destructive long waves generated by various sources under the sea surface (e.g., earthquakes, submarine landslides and/or volcanic eruptions) or above the sea surface (e.g., meteorological events, asteroid impacts). While tsunamis generated by earthquakes and landslides have been studied immensely, there is less focus on research related to meteotsunamis (tsunamis of meteorological origin) as they are considered as rare and underrated phenomenon (Pattiaratchi and Wijeratne 2015; Rabinovich 2020). Meteotsunamis are long waves generated by a displacement of a water body due to atmospheric pressure disturbances and often have local names such as "Rissaga" (Balearic Islands), "Marubbio" (Sicily), "Milghuba" (Malta), "Abiki" (Nagasaki Bay) and "Seebär" (Baltic Sea) (Monserrat and Rabinovich 2006).

Long ocean waves of meteorological origin have been observed and described in the scientific literature at the following locations around the world; USA East Coast (Churchill et al. 1995; Sallenger et al. 1995; Pasquet and Vilibić 2013; Lipa et al. 2014), Gulf of Mexico (Paxton and Sobien 1998), The Great Lakes (Ewing et al. 1954; Donn 1959; Bechle and Wu 2014), Atlantic Ocean (Mercer 2002; Candella 2009; Dragani et al. 2009), Adriatic Sea (Vučetić et al. 2009; Šepić et al. 2012), Mediterranean (Airy 1878; Monserrat et al. 1991; Rabinovich and Monserrat 1996; Vilibić et al. 2008), the Aegean Sea (Papadopoulos 1993), Black Sea (Vilibić et al. 2010), East China Sea (Hibiya and Kajiura 1982; Tanaka 2010), Sea of Japan (Park 1986) and Yellow Sea (Wang et al. 1987; Cho et al. 2013). Moreover, Pattiaratchi and Wijeratne (2015) listed meteotsunami events around the world according to maximum wave heights, and recently Rabinovich (2020) overviewed 49 known events to illustrate the origin of these waves and their correlation to atmospheric disturbances. He also classified these meteotsunami events based on good or bad weather conditions as well as their location of impact. One or a few solitary waves are observed on open coasts such as along straight beaches, whereas more intense harbor oscillations are observed in embayments.

General characteristics of meteotsunamis are similar to those of tsunamis of tectonic or landslide origin. They have similar spatial scales with landslide tsunamis due to being local events, whereas temporal scales of several minutes to hours are common for all of them. These tsunami waves may cause devastating destructions in the coastal zone (Monserrat et al. 2006). The difference is in the mechanisms of their generation. For meteotsunamis, sources are spatial and temporal pressure distributions, atmospheric gravity waves and squall lines (Rabinovich 2020). However, in order to be noticeable, meteotsunamis require amplification as the equilibrium response to atmospheric pressure variations (inverted barometer principle) can only generate a few centimeters of water level change (Romero et al. 2019).

There have been several studies focused on the mechanisms of meteotsunami generation and propagation. Some researchers also used analytical and numerical models to analyze the mechanism of ocean wave generation by atmospheric pressure disturbances under idealized conditions. Vilibić (2008) simulated the Proudman resonance caused by sinusoidal air pressure disturbances. He also discussed the similarities between meteotsunamis and landslide tsunamis as both mechanisms generate forced waves and free waves, which then propagate along the ocean surface. A series of analytical studies on the trap and refraction of ocean waves induced by moving atmospheric pressure over a step bottom and continental shelf were conducted by Vennell (2007, 2010), Thiebaut and Vennell (2011) and Melinand (2015). Niu and Zhou (2015) studied the shape of water surface oscillations under a

moving low-pressure system with different speeds by adopting a nonlinear shallow water model. They used a moving low pressure with Gaussian distribution in an unbounded flat-bottom water area and analyzed the effects of speed, central pressure drop and spatial scales on the water elevation. Choi and Seo (2017) investigated the ocean waves induced by a low-pressure system moving over a slope towards shore based on an idealized problem from the landing process of a typhoon or a hurricane. They also investigated the runup and development of edge wave patterns generated by a moving a circular shape atmospheric pressure disturbance across a straight shoreline on a sloping beach. A Gaussian shape pressure drop of 20 hPa is used at the center in the circular area of a 200 km radius. Various speeds of pressure disturbance are selected up to 50 m/s and tested. The change in the maximum runup is presented according to different moving speeds for the given atmospheric pressure disturbance. While wave runup and rundown are repeated at the shoreline, the generation and propagation of edge waves in the alongshore direction due to wave refraction are also observed.

In this study, the atmospheric pressure disturbance acts on the water surface and generates free and forced waves, which are amplified due to the Proudman resonance and shoaling. Similarly, Chen and Niu (2018) focused on the occurrence of Proudman resonance when the speed of moving pressure disturbance is close to the local shallow water wave velocity (celerity) as the disturbance moves to the shore over a slope. They performed a numerical investigation on the generation and propagation of forced waves induced by a circular shape atmospheric pressure drop. The wave pattern evolves from a concentric-circle type into a triangular type with the increase in the Froude number on the slope, which can be defined as $Fr = V/c$; the ratio of the atmospheric pressure speed, V, to the celerity of long ocean waves $c = \sqrt{gh}$ where g is the gravitational acceleration and h is the water depth. The effects of the characteristic parameters of the circular pressure disturbances and slope gradient are discussed. They found that it is not always possible to observe the significant peak of the maximum water elevation before the landing of pressure disturbances. The extremely high runup is observed when the forced wave hits the shore. In another recent study, Niu and Chen (2020) state that energy is transferred from the atmosphere to the ocean during the response of the sea to a disturbance, while the forced wave induced by the disturbance gradually grows and finally reaches a quasi-steady state. The time required to excite the forced wave induced by pressure disturbance as it reaches a steady state is quantified based on the nonlinear shallow water wave model by Niu and Chen (2020).

Many meteotsunami events are reproduced by numerical modeling with different degrees of accuracy (Rabinovich et al. 1999; Liu et al. 2003a; Vilibić et al. 2004,2008; Dragani, 2007; Orlić et al. 2010; Tanaka, 2010; An et al. 2012; Bechle and Wu, 2014; Šepić et al. 2018; Heidarzadeh et al. 2020). Romero et al. (2019) state that a simple shallow water model may suffice to represent the dynamics and amplification of long ocean waves provided the atmospheric coupling and resonant mechanisms are accounted for. Much of the research on meteotsunami modeling uses available numerical ocean models that utilize Navier–Stokes equations with hydrostatic and Boussinesq approximations. Romero et al. (2019) use shallow water equations after the inclusion of the appropriate atmospheric forcing term, and they include a drag force in the momentum equation to integrate bottom roughness and seabed frictional resistance. Šepić et al. (2018) use an ocean model code developed by Dr. Isaac Fine (Institute of Ocean Sciences, Sidney, BC) to simulate Odessa meteotsunami based on depth-integrated shallow water equations with Coriolis term and all nonlinear terms, except bottom friction, omitted. In this code, the time derivative of air pressure is a principal input parameter and it is independent of other model outputs and parameters. Bubalo et al. (2018) simulate Chrystal and Proudman resonances in a closed

rectangular basin with two finite element (ADCIRC and SCHISM) models and one finite difference (ROMS) ocean model. They state that even though all three models are solving the same equations with similar approximations, there is a substantial difference in time-stepping integration technique between them, and the Courant–Friedrichs–Levy (CFL) condition becomes important when these models are used to describe Proudman resonance as accurately as possible. They conclude that the errors that may arise from choosing an inadequate integration time step for all areas of the grid may be very significant and affect the quality of the results of Proudman resonance in the open sea, which will, therefore, affect the reproduction in coastal areas.

Denamiel et al. (2019) discuss the challenges in meteotsunami modeling, stating that resolution and bathymetry used in ocean models, as well as meteorological forcing, are not accurate enough to truly recreate the generation, propagation, and amplification of these events. Following the experiences of many researchers (Monserrat et al. 2006; Tanaka, 2010; Horvath and Vilibić, 2014), they conclude that while the main challenge is reproducing the atmospheric physics responsible for creating the atmospheric disturbances, the development of reliable atmospheric-ocean coupled models for the short-term forecast is also important. They recommend that for an ocean model to capture the offshore meteotsunami dynamics, the atmospheric forcing should be imposed every minute to capture the speed and amplitude of pressure disturbances, and the spatial resolution should allow for an accurate representation of the continental shelf. However, Denamiel et al. (2019) conclude that spatial discretization and lack of precise bathymetric data limits the accuracy of the present state-of-the-art ocean numerical models to represent the ocean and complex geomorphology of the coast responsible for the meteotsunami wave generation and amplification (Proudman and topographic resonances). Their discussion focuses on the operation of a regional meteotsunami system developed for the Adriatic region and aims to work in real-time for early warning and forecasting purposes.

For the ocean, Proudman and topographic resonances are the main generation and amplification processes of long oceanic waves (Monserrat et al. 2006; Vennell, 2010). Due to spatial discretization and lack of precise bathymetric data, it is unlikely that present state-of-the-art ocean numerical models can accurately represent the ocean and coast complex geomorphology responsible for the meteotsunami wave generation and amplification, which is particularly true for the middle and southern parts of the eastern Adriatic. However, given these overwhelming limitations, the AdriSC Meteotsunami Forecast component is showing skills in fair reproduction of meteotsunami events, which might be used for operational forecasting.

Bubalo et al. (2019) attempted to improve the numerical simulations by including the flooding and drying option of a finite element model (ADCIRC) for Adriatic since many of the previous studies either had cut-off depths set at several meters or did not utilize flooding and drying option. They also state that flooding and drying are not frequently used in meteotsunami studies, contrary to storm surge and tsunami research. They show that the inclusion of flooding and drying leads to a much more accurate reproduction of the event and grid refinement is very important as well. They recommend the use of a flooding and drying algorithm for modeling meteotsunami events.

This paper presents the new module of NAMI DANCE tsunami numerical code that solves the nonlinear shallow water equations with the air pressure forcing term to simulate meteotsunamis. An ocean model should capture both the offshore generation and resonant amplification of meteotsunamis, and the nearshore amplification of the tsunami-like wave by topography and harbor resonance (Rabinovich 2009). Based on the vast validation of NAMI DANCE model, the nearshore amplification process of tsunami waves has

already been satisfied, including harbor resonance. Yalciner and Zaytsev (2017); Lynett et al. (2017) and Dogan et al. (2021) are some of the works that present the capability of NAMI DANCE model in properly representing the nearshore amplification process due to topography applied in various tsunami events. The performance of NAMI DANCE model to represent harbor resonance and the amplification process of long waves are presented in Sozdinler et al. (2015); Yalciner et al. (2015) and Sogut and Yalciner (2019). The previous applications of NAMI DANCE model include the tsunami waves generated by earthquakes and landslides. The additional module to solve generation, propagation and coastal amplification of the ocean waves due to spatial and temporal change of pressure and wind fields is introduced in this paper. The cases simulated in this paper provides validation of NAMI DANCE by comparing the numerical results with analytical solutions and show that it is capable of modeling the generation, propagation, and coastal amplification of ocean waves and Proudman resonance due to moving atmospheric disturbances.

2 Resonance by coupling of ocean wave motion and atmospheric pressure forcing

When the air pressure decreases gradually, the water level in the sea region rises in the order of 1 cm with respect to 1 hPa pressure decrease. The water level changes can be amplified by the resonance when the ocean wave speed coincides with the speed of the atmospheric pressure disturbance. The three most important resonance mechanisms are (i) Proudman resonance (Proudman, 1929), (ii) Greenspan resonance (Greenspan, 1956) and (iii) shelf resonance (Monserrat et al. 2006).

Pattiaratchi and Wijeratne (2015) specified that Proudman resonance is the main cause of meteotsunamis happening all over the world. Proudman resonance occurs when the velocity (V) of the atmospheric pressure movement coincides with the celerity (c) of the ocean wave, which denotes $V = c$. The changes in the water surface level due to air pressure disturbances depend on the Froude number (Fr). Šepić et al. (2015) stated that when $Fr \approx 1.0$, during movement of the ocean waves, atmospheric energy is absorbed and, therefore, strong amplification occurs.

Greenspan resonance occurs where the air pressure velocity in alongshore direction (V_l) is close to the propagation phase speed of j-th mode of edge waves (c_j). The generated edge waves amplify due to Greenspan resonance in relation to the amplitude and the propagation speed of the pressure disturbance and a beach slope.

The atmospheric pressure disturbance causes the initial change in water level, and water oscillations develop due to the shelf geometry such as length, water depth, topographic funneling, and bed slope. Shelf resonance occurs when the period or wavelength of atmospherically induced ocean waves and waves in the continental shelf region coincide.

The internal resonance mechanism has another important role in wave amplification inside enclosed basins and harbors. When the natural resonance frequency of a semi-enclosed basin coincides with the frequency of incoming wave or forcing to the basin, then strong amplification can be observed inside the basin. A short cut numerical method for the determination of periods of free oscillations for basins with irregular geometry and bathymetry is presented in Yalciner and Pelinovsky (2007). Bailey et al. (2014) stated that in long, narrow, and shallow bays, stronger oscillations occur while the system tends to have a low rate of energy dissipation.

3 Problem and method

3.1 Wave generation and propagation due to atmospheric pressure disturbances

The energy transfer in the oceans by ocean waves is generally categorized according to the energy sources such as wind, fault break, submarine or subaerial landslides, pressure disturbance, or solar and planetary attractions. Air pressure disturbances cause water level changes and hence generate long-period ocean waves. High atmospheric pressure causes a static water level drop and contrariwise, low atmospheric pressure causes a static water level rise. Due to the different water level changes at high pressure and low pressure regions, the water level differences cause the wave generation in the sea, and consequently, propagation and coastal amplification in the ocean area.

On the other hand, bathymetry is an important factor that may cause amplification of the long waves generated by atmospheric pressure disturbance. The speed of pressure disturbance (V) and wave celerity (c) are the two important parameters that govern the characteristics of the generated long waves. The speed of the ocean waves is controlled by the water depth and it may be faster or slower or equal to the speed of pressure disturbance. Therefore, the shape and propagation of the generated ocean waves differ according to the different speeds of pressure disturbances as well as the magnitude and gradient of the pressure disturbance. In this study, the effects of the speed of pressure disturbance on the generation, propagation and amplification of the ocean waves in the basins with different bathymetries are investigated.

Simple analytical solutions for long wave generation in a basin of constant depth (Proudman resonance) and a basin with a linear sloping bottom (Greenspan resonance) are given in their original papers (Proudman 1929; Greenspan 1956) and then reproduced in many papers. This paper aims to define the analytical solution of the linear shallow water model and compare the results with the numerical solution of the linear and nonlinear shallow water model. Thereafter, analytical and numerical models are applied to certain test cases. This helps to interpret the verification of the numerical model and the wave generation and propagation mechanism due to the speed of pressure disturbances over different types of basins.

3.2 Analytical solution

The governing equations for tsunami wave generation by atmospheric disturbances in narrow bays and channels can be written similar to the 1D case studied for tsunami landslide generation (Tinti et al. 2001; Tinti and Bortolucci 2000; Liu et al. 2003b; Pelinovsky, 2006; Didenkulova et al. 2010; Didenkulova and Pelinovsky, 2013):

$$\frac{\partial S}{\partial t} + \frac{\partial}{\partial x}(uS) = 0 \tag{1}$$

$$\frac{\partial u}{\partial t} + u\frac{\partial u}{\partial x} + g\frac{\partial H}{\partial x} = -\frac{1}{\rho}\frac{\partial p_{atm}}{\partial x} \tag{2}$$

where $H(x, t)$ is the water depth along the channel axis, $u(x, t)$ is the flow velocity averaged over a cross section, g is the gravity acceleration, $S(H, x, t)$ is the variable cross section of the bay filled by water, $p_{atm}(x,t)$ is atmospheric pressure, ρ is the density of the water, x is coordinate, and t is time. Resonant amplification of tsunami waves induced by moving landslides is studied in (Didenkulova et al. 2011; Didenkulova and Pelinovsky 2012).

Generated ocean waves and the atmospheric disturbance are assumed to be uniform over the cross section.

In the important case of the quasi-parabolic channel, its cross section is described by

$$z \sim |y|^m \tag{3}$$

where m is an arbitrary positive constant. In particular, $m = 1$ describes the triangular channel, $m = 2$ describes the parabolic channel, and $m \to \infty$ corresponds to the rectangular channel. As a result, we may compute a function $S(H)$

$$S(H) = \int_{-y_0}^{+y_0} z(y)dy \sim H^{(m+1)/m} \tag{4}$$

For such channels, we have Eqs. (1) and (2) for wave components:

$$\frac{\partial H}{\partial t} + u\frac{\partial H}{\partial x} + \frac{m}{m+1}H\frac{\partial u}{\partial x} = 0 \tag{5}$$

$$\frac{\partial u}{\partial t} + u\frac{\partial u}{\partial x} + g\frac{\partial H}{\partial x} = -\frac{1}{\rho}\frac{\partial p_{atm}}{\partial x} \tag{6}$$

The set of analytical solutions can be obtained if the atmospheric disturbance is weak. In this case, we may use the linear version of these equations

$$\frac{\partial \eta}{\partial t} + \frac{m}{m+1}h\frac{\partial u}{\partial x} = 0 \tag{7}$$

$$\frac{\partial u}{\partial t} + g\frac{\partial \eta}{\partial x} = -\frac{1}{\rho}\frac{\partial p_{atm}}{\partial x} \tag{8}$$

where $\eta(x, t) = H(x, t) - h$ is the vertical displacement of the water surface, and h is an unperturbed water depth along the longitudinal axis.

This system can be reduced to the wave equation

$$\frac{\partial^2 \eta}{\partial t^2} - c^2\frac{\partial^2 \eta}{\partial x^2} = \frac{c^2}{\rho g}\frac{\partial^2 p_{atm}}{\partial x^2} \tag{9}$$

where

$$c = \sqrt{\frac{m}{m+1}gh} \tag{10}$$

where c is the wave celerity in the channel. It is important to note that Eq. (9) has a universal form for waves in channels of any quasi-parabolic shape; the channel shape is described by the coefficient m in Eq. (10). Namely, this equation is studied for describing the Proudman resonance (Melinand, 2015).

By introducing

$$\zeta_a = \frac{p_{atm}}{\rho g} \tag{11}$$

Equation (9) can be rewritten in the following form

$$\frac{\partial^2 \eta}{\partial t^2} - c^2 \frac{\partial^2 \eta}{\partial x^2} = c^2 \frac{\partial^2 \zeta_a}{\partial x^2} \tag{12}$$

In particular, the response on the static atmospheric disturbance is described by the well-known "inverse barometer law."

$$\eta = -\zeta_a = -\frac{p_{atm}}{\rho g} \tag{13}$$

It means that low atmospheric pressure can cause the sea level rise, and high atmospheric pressure leads to depression in the mean sea level. If the pressure is moving, the resonance can occur when the pressure velocity is close to the wave celerity. Then, replacing

$$\eta = \zeta - \zeta_a \tag{14}$$

we may transform Eq. (12) to

$$\frac{\partial^2 \zeta}{\partial t^2} - c^2 \frac{\partial^2 \zeta}{\partial x^2} = \frac{\partial^2 \zeta_a}{\partial t^2} \tag{15}$$

In this form, Eq. (15) coincides with those used for tsunamis generated by landslides (Tinti et al. 2001; Liu et al. 2003b; Pelinovsky, 2006; Didenkulova et al. 2010; Didenkulova and Pelinovsky, 2013).

Initial conditions for the shallow water system (7–8) are applied to both $\eta(x, t)$ and $u(x, t)$. If at the initial moment the ocean rests, they can be transformed into conditions for the function $\eta(x, t)$

$$\eta(x, 0) = 0, \ \frac{\partial \eta}{\partial t}(x, 0) = 0 \tag{16}$$

The linear Eq. (15) with initial conditions (16) can be solved using the Duhamel's integral

$$\eta(x, t) = \frac{c}{2\pi} \int_0^t d\tau \int_{x-c(t-\tau)}^{x+c(t-\tau)} dy \frac{\partial^2 \zeta_a(y, \tau)}{\partial y^2} \tag{17}$$

which can be integrated once

$$\eta(x, t) = \frac{c}{2\pi} \int_0^t d\tau \left(\frac{\partial \zeta_a[x + c(t - \tau), \tau]}{\partial x} - \frac{\partial \zeta_a[x - c(t - \tau), \tau]}{\partial x} \right) \tag{18}$$

This solution can be used for the control of numerical computations. If the atmospheric disturbance moves with a constant velocity, V, the solution (18) becomes algebraic

$$\eta(x, t) = \frac{Fr^2}{Fr^2 - 1} \zeta_a(x - Vt) - \frac{Fr^2}{2(Fr - 1)} \zeta_a(x - ct) + \frac{Fr^2}{2(Fr + 1)} \zeta_a(x + ct) \tag{19}$$

where

$$Fr = \frac{V}{c} \qquad (20)$$

is the Froude number. The wave celerity varies with the water depth, and Fr varies with the speeds of pressure disturbance and generated water waves.

The response to the moving disturbance represents three waves. The first term in Eq. (19) describes the forced wave, which propagates together with the atmospheric disturbance. The forced wave can have different polarities depending on the regime of the disturbance motion. Assuming ζ_a is positive, the forced wave is positive in the super-critical regime ($Fr > 1$) and negative in the sub-critical regime ($Fr < 1$). The second term describes a free wave, which propagates with its own speed c. As the forced wave, it can also be of different polarities: negative in the super-critical regime and positive in the sub-critical regime. The last term corresponds to the free wave of positive polarity. It is important to mention that the solution (19) has the same form for waves generated by a landslide moving with constant speed in a basin of constant depth (Tinti et al. 2001; Pelinovsky, 2006), for 1D landslide moving along the non-reflecting bottom profile $h \sim x^{4/3}$ (Didenkulova et al. 2010) and along narrow bays of variable cross sections (Didenkulova and Pelinovsky, 2013).

For practice, it is useful to compare amplitudes of waves moving in the same direction as an atmospheric disturbance. The ratio of the amplitude (Q) of the free wave (second term) to the amplitude (P) of the forced wave (first term) is

$$\frac{Q}{P} = \frac{Fr + 1}{2} \qquad (21)$$

The general sectional view of long waves generated by moving constant atmospheric pressure is shown in Fig. 1 for the case Fr < 1.

Formula (21) is correct for any Fr. But for $Fr < 1$, it is the ratio of the front wave to the rear wave (forced wave is behind the free wave), as shown in Fig. 1. For $Fr > 1$, the forced wave is in front of the free wave, and therefore, Eq. (21) gives the ratio of the rear wave to the front wave.

Fig. 1 A schematic view of the moving constant low atmospheric pressure (plan view, top) and the general sectional view of long waves (bottom), propagating in the direction of the pressure
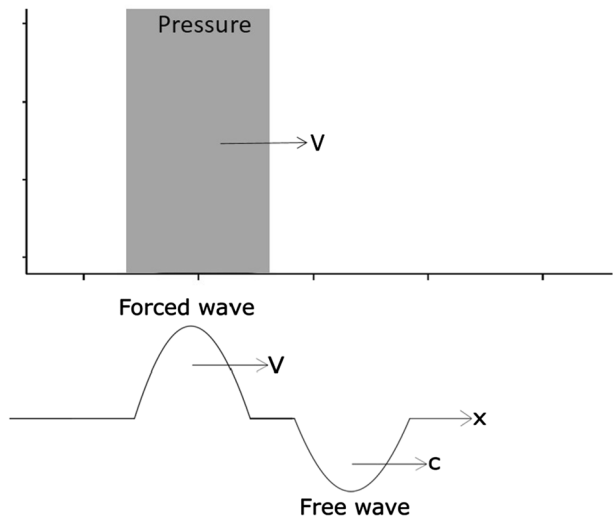
In the case of resonance ($Fr=1$), the solution (19) transforms into

$$\eta(x,t) = -\frac{t}{2}\frac{\partial \zeta_a(x-ct)}{\partial x} + \frac{1}{4}\zeta_a(x+ct)$$

(22)

and wave amplitude increases with time.

3.3 Numerical model

Atmospheric pressure disturbances on the water body may induce long waves. The three distinctions are important for the long waves: i) generation of the wave, ii) propagation of the wave in deep water, and iii) propagation and coastal amplification in shallow water and on the shore. Wave propagation in deep water can be explained by the linear shallow water equations. In contrast, in shallow water, wave dynamics is better described by the nonlinear shallow water equations, which also cover the surface and bottom stresses, Coriolis force, and shoaling (Eze et al. 2009). A full potential model or Boussinesq-type equations are even better in shallower regions. Several numerical models were tested and compared in Liu et al. (2008) and Lynett et al. (2017). Some of those numerical codes are COMCOT (Liu et al. 1994; 2008), TUNAMI-N2 (Imamura 1996; Imamura et al. 2006; Liu et al. 2008), MOST (Titov and Synolakis, 1998; Liu et al. 2008; Lynett et al. 2017), NAMI DANCE (Liu et al. 2008; Sozdinler et al. 2015; Yalciner and Zaytsev 2017; Metin 2016; Lynett et al. 2017; Sogut and Yalciner 2019; Dogan et al. 2021), which use shallow water wave equations, while FUNWAVE (Kirby et al. 1998) and GEOWAVE (Watts et al. 2003) use Boussinesq-type equations. The aforementioned numerical models are developed for the numerical solution of co-seismic and/or landslide generated tsunamis without considering the atmospheric pressure disturbance.

In the present study, the nonlinear shallow water equations containing the air pressure forcing and wind field forcing terms are solved numerically to simulate generation, propagation and coastal amplification of long waves generated by the atmospheric pressure disturbances and wind field forcing. In this direction, NAMI DANCE is upgraded to the new version called NAMI DANCE SUITE with the capability of using the Graphical Processing Unit of the graphic card. It computes the main hydrodynamic parameters of long waves, which are (i) maximum positive amplitude, (ii) maximum flow depth, (iii) maximum current velocity, (iv) maximum momentum flux, (v) maximums hydrodynamic forces, (vi) maximum negative amplitude, (vii) maximum wave arrival time, (viii) initial wave arrival time and (ix) durations of inundation and shoreline withdrawal (Yalciner et al. 2015,2017; Sozdinler et al. 2015; Yalciner and Zaytsev 2017).

The set of two-dimensional equations with atmospheric pressure and wind field terms in Cartesian coordinates are given in Eqs. (23)-(25):

$$\frac{\partial \eta}{\partial t} + \frac{\partial M}{\partial x} + \frac{\partial N}{\partial y} = 0$$

(23)

$$\frac{\partial M}{\partial t} + \frac{\partial}{\partial x}\left(\frac{M^2}{D}\right) + \frac{\partial}{\partial y}\left(\frac{MN}{D}\right) + gD\frac{\partial \eta}{\partial x} + \frac{\tau_x}{\rho_w} + \frac{D}{\rho_w}\frac{\partial P_{atm}}{\partial x} - \frac{\rho_{air}C_D}{\rho_w}U_{w10}\sqrt{U_{w10}^2 + V_{w10}^2} = 0$$

(24)

$$\frac{\partial N}{\partial t} + \frac{\partial}{\partial x}\left(\frac{MN}{D}\right) + \frac{\partial}{\partial y}\left(\frac{N^2}{D}\right) + gD\frac{\partial \eta}{\partial y} + \frac{\tau_y}{\rho_w} + \frac{D}{\rho_w}\frac{\partial P_{atm}}{\partial y} - \frac{\rho_{air}C_D}{\rho_w}V_{w10}\sqrt{U_{w10}^2 + V_{w10}^2} = 0$$

(25)

where t is time; x and y are spatial coordinates in West–East and South-North directions, respectively; η is the water surface elevation; ρ_w is the water density; ρ_{air} is the air density; D is the water depth, P_{atm} is the atmospheric pressure in Pascal; τ_x and τ_y are the bottom shear stresses; U_{w10} and V_{w10} are wind velocities at 10 m elevation in x and y directions; C_D is the wind drag coefficient computed by the following equations (Garrat 1977; Powell et al. 2003):

$$C_D = (0.75 + 0.067(U_{w10} - u)) \cdot 10^{-3} \text{ for } U_{w10} \leq 26 \text{ m/s} \tag{26}$$

$$C_D = 2.18 \cdot 10^{-3} \text{ for } U_{w10} \leq 26 \text{ m/s} \tag{27}$$

where M and N are the discharge fluxes in the x and y directions:

$$M = \int_{-h}^{\eta} u\,dz = u(D + \eta) = uD, \ N = \int_{-h}^{\eta} v\,dz = v(D + \eta) = vD \tag{28}$$

In Eq. (28), u and v are the water current velocities in x and y directions (horizontal plane), respectively. The bottom shear stresses are computed using Eqs. (29) and (30).

$$\frac{\tau_x}{\rho} = \frac{f_b n^2}{(\eta + D)^{\frac{7}{3}}} M \sqrt{M^2 + N^2} \tag{29}$$

$$\frac{\tau_y}{\rho} = \frac{f_b n^2}{(\eta + D)^{\frac{7}{3}}} N \sqrt{M^2 + N^2} \tag{30}$$

where f_b denotes the bottom friction, which is 0.015, and Manning's coefficient n is calculated by

$$n = \sqrt{\frac{f_b(\eta + D)^{\frac{1}{3}}}{2g}} \tag{31}$$

Since Coriolis force and friction are not included in the analytical solution, those are not included in the numerical tests for proper comparisons with the analytical solution.

In the numerical model, in addition to standard inputs (bathymetry, initial water surface displacement, and fluxes if needed), the spatial distribution of the barometric pressure at the sea level in Pascal at one-minute intervals during the simulations is employed. As a set of output parameters, NAMI DANCE SUITE computes water surface elevations, magnitude and directions of water current velocities, momentum fluxes, overland flow depths throughout the domain at specified time intervals, and extremums of all these parameters. Additionally, the inundation and withdrawal limits of the shoreline motion; and time histories of these parameters at specified numerical wave gauge locations are computed.

3.4 Verification of the model

In order to verify the model to correctly calculate the long wave motion due to the effects of atmospheric pressure disturbances, the test simulations are conducted with a regular shaped flat bathymetry (200 km of distance between 0.9 W and 0.9E longitudes, 195 km of distance between 0.885S and 0.885 N latitudes and 200 m of constant depth). The North

and South boundaries of the basin are used as solid impermeable boundaries in order to prevent the escape of waves through these borders. The East and West borders are open (outgoing) boundaries. The 16 km wide high pressure disturbance (102,000 Pa) propagating with a constant velocity from West to East is used in all simulations. The standard pressure over the basin is set as 100,000 Pa. The borders of the pressure disturbance are smoothed by the 2 km linear increase from and decrease to 100,000 Pa at the front and rear sides of the disturbance (Fig. 2). The selected pressure disturbance band is an exceptional case. The main reason to select this disturbance is to obtain higher water fluctuations for a better comparison of the simulation results.

For verification of the model, a flat bottom basin is selected where the wave celerity is constant and is equal to $c = 44.3$ m/s. Different constant speeds (V) of pressure disturbance are selected as 11 m/s, 22 m/s, 33 m/s, 44 m/s, 55 m/s, 66 m/s. Therefore, both sub-critical, critical and super-critical conditions defined by Eq. (20) are used. The spatial grid size and time step are selected as 177 m and 1 s, respectively. The bottom friction, f_b, is selected as zero to satisfy the same friction condition with the analytical solution. The duration of each simulation is set according to the duration of the ocean wave and pressure disturbance propagation to leave the right boundary of the basin.

The distributions of water surface (sea states) and sectional views at zero latitude at selected time steps ($t = 10$ min, 20 min, 40 min and 60 min) over flat bottom basin under pressure disturbance moving with 22 m/s, 44 m/s and 66 m/s speed are presented in Fig. 3.

To verify the accuracy of the numerical model, the simulations are performed for six different Froude numbers. The ratios of the amplitude of the free wave (determined by the wave celerity) to the amplitude of the forced wave (determined by the speed of pressure disturbance) are computed and compared with the analytical predictions (see Table 1). In the numerical simulations for comparison and validation with the analytical solution, the linear wave equations are used. The comparisons show that the majority of the % Error (the ratio of the absolute difference between numerical results and the corresponding analytical results) for each Fr is less than 1%. Furthermore, the same simulations are performed using different grid sizes of 50 m, 100 m, 177 m, 354 m and 708 m for the sensitivity analysis due to the grid size. The numerical results for Fr = 1 indicate that no significant difference occurred with changing grid size in the range of used sizes with a % Error less than 1.5%.

Fig. 2 The top and sectional view of the pressure disturbance at the beginning of the simulation ($t = 0$)
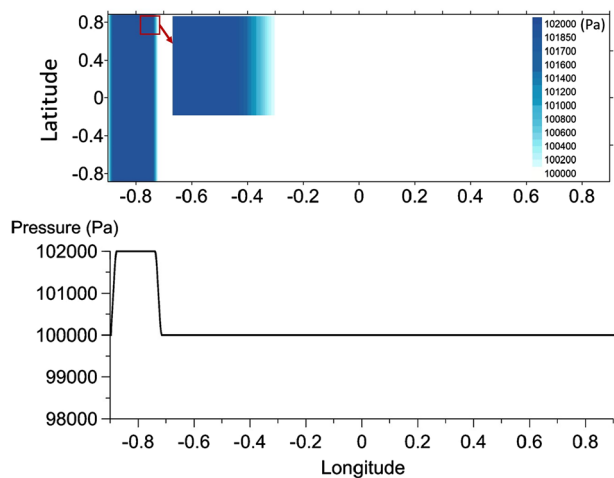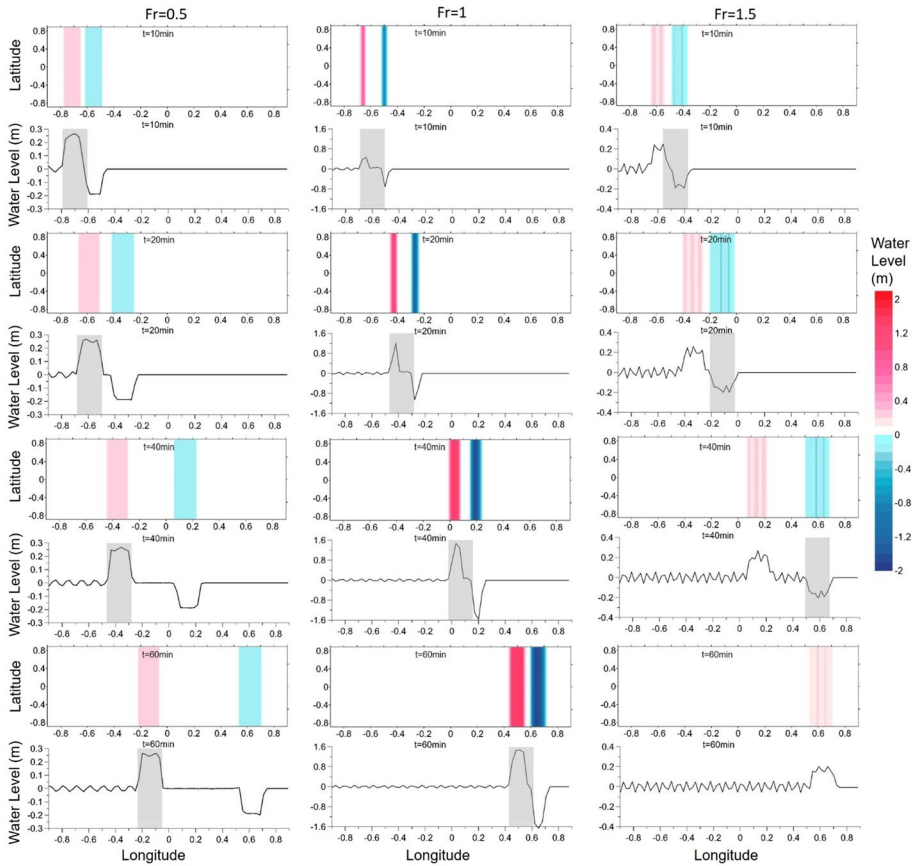
Fig. 3 The sea state at $t = 10$ min, 20 min, 40 min, 60 min for the pressure disturbance moving with 22 m/s (left column), 44 m/s (middle column) and 66 m/s speed (right column) over 200 m deep flat bottom basin. Rows 1, 3, 5 and 7 show top view; rows 2, 4, 6 and 8 show sectional view of the water surface at zero latitude (note, vertical scales of sectional views are different). The grey shaded area is the location of the pressure disturbance band at the respective time

Table 1 Amplitude ratios (Q/P) of the numerical and analytical results for 200 m deep flat bottom basin ($c = 44.3$ m/s, grid size dx = 177 m and $f_b = 0$)

Speed of pressure disturbance V (m/s)	Fr	Absolute ratio of the amplitudes of free wave to forced wave		% Error
		Analytical	Numerical	
11	0.25	0.624	0.622	0.3%
22	0.50	0.748	0.752	0.5%
33	0.75	0.873	0.877	0.5%
44	1	1	0.999	0.1%
55	1.25	1.121	1.114	0.6%
66	1.5	1.245	1.272	2.1%

4 Numerical tests for different types of basins

The investigation of the long wave generation and propagation due to the moving pressure disturbance with a constant speed is important to understand considering the possible wave amplification at shallow regions in relation to bathymetric and morphologic conditions in basins and/or marine environment. In this direction, three different basins are selected for applications with different cross sections in lateral or longitudinal directions with respect to directions of pressure disturbance and ocean wave; (i) triangular lateral cross section, (ii) stepwise shelf from 200 to 20 m of depth on 1:10 slope in the longitudinal direction, (iii) stepwise shelf from 200 to 20 m of depth on 1:700 slope in the longitudinal direction. Additionally, similar stepwise shelf basins on slopes varying from 1:100 to 1:600 are simulated to expand the numerical tests over different slopes.

4.1 Simulations in the basin with triangular cross section

The basin with a triangular cross section has a 200 m water depth at the center along the direction of pressure disturbance with 1:444 side slopes. The top and sectional views of the basin are given in Fig. 4. According to Eq. 10, the representative wave celerity of this basin becomes 31.3 m/s, which is calculated with a reference depth of 200 m and $m=1$. Simulations are performed using three different speeds of the pressure disturbance (22 m/s, 31 m/s and 44 m/s) or Fr (0.7, 1, and 1.4) propagating over the basin with the triangular cross section.

The distributions of water surface (sea states) and sectional views at zero latitude at selected time steps ($t=10$ min, 20 min, 40 min and 60 min) under the moving pressure disturbance with 22 m/s, 31 m/s and 44 m/s speeds in the basin with triangular cross section are presented in Fig. 5.

For three different speeds of pressure disturbance, the maximum wave amplification is observed for the case of 44 m/s speed of pressure disturbance at 200 m depth, the deepest part (along the central axis) of the basin. A similar wave amplification was observed for the case of 31 m/s speed of the pressure disturbance, which coincides with the corresponding speed of the free wave at about 94 m water depth. In the case of $V=22$ m/s, the extrema of positive and negative amplitudes are less compared to the other two cases observed at a depth of ~ 49 m.

4.2 Simulations in the basin with stepwise shelf bathymetry

Several different basins with stepwise shelf bathymetry are used for the other sets of simulations. The selected basins are composed of three parts as; i) 200 m deep flat bottom, ii) a sloping connection from 200 m depth to 20 m depth, and iii) 20 m deep flat bottom. The slopes considered in section (ii) are selected as 1:10 and 1:700 for two different cases. As

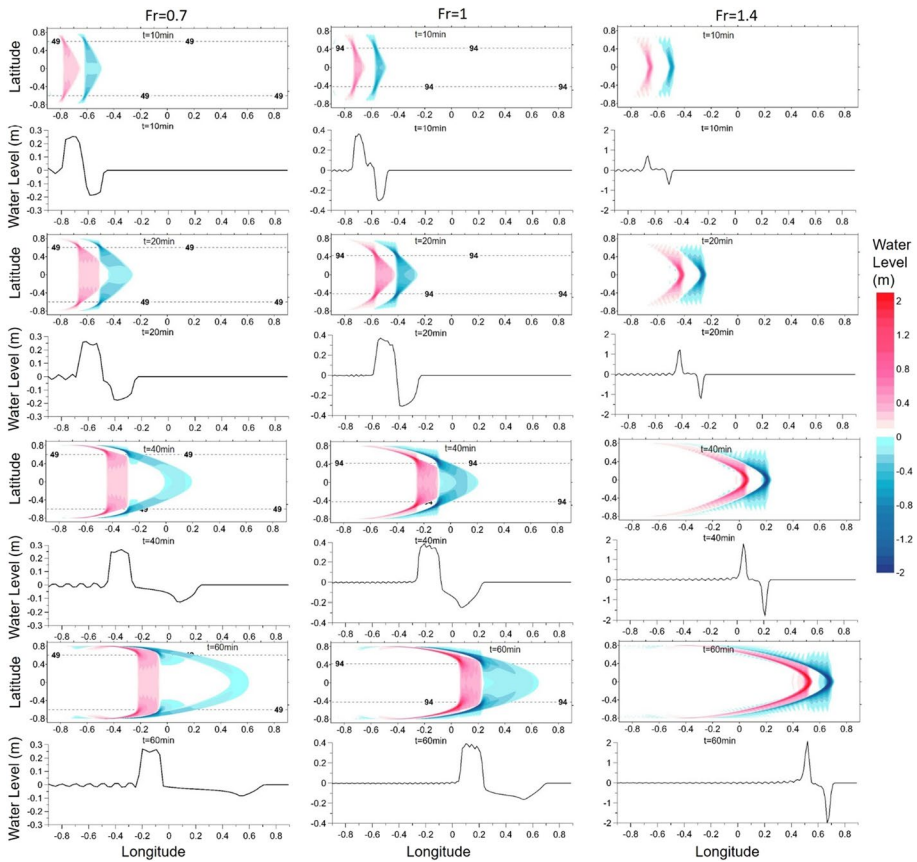**Fig. 4** Top and sectional (along section A-A) views of the triangular basin
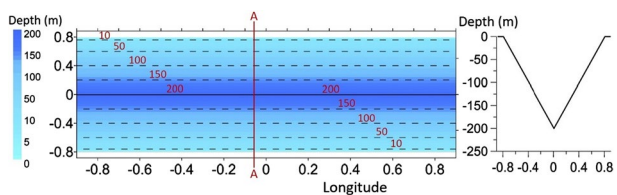
Fig. 5 The sea state at $t = 10$ min, 20 min, 40 min, 60 min for the pressure disturbance moving with the speed of 22 m/s (left column), 31 m/s (middle column) and 44 m/s (right column) in the basin with triangular cross section. Rows 1, 3, 5 and 7 show top views; rows 2, 4, 6 and 8 show sectional views of the water surface at zero latitude (note, vertical scales of sectional views are different). The black dashed lines show water depths of 49 m in the first, 94 m in the second and 200 m in the last column

before, the basins at the Northern (top) and the Southern (bottom) boundaries are used as solid impermeable boundaries to prevent the lateral escape of energy from these boundaries. The East and West borders are open (outgoing) boundaries. The simulations are performed using three different speeds of pressure disturbance (22 m/s, 31 m/s and 44 m/s) propagating over the basins with stepwise shelf bathymetry. The results for the two different basins are given in the following sections. In addition, six different slopes varying from 1:100 to 1:600 are also numerically tested for 31 m/s speed of pressure disturbance to elaborate on the effect of slope in section (ii) on wave amplification. The results of these simulations show that as the slope becomes milder, there is an increase in the extrema of the positive and negative wave amplitudes during the 120 min simulation (the row indicated with a star symbol in Table 2). The amplification in the amplitudes of the depression (front part) and the elevation (rear part) waves is also higher for a milder slope but observed at different time steps of the simulation depending on the location of the slope (bold amplitude values in Table 2).

4.2.1 Stepwise shelf bathymetry with 1:10 shelf slope

The top and sectional views of the stepwise shelf bathymetry with 1:10 shelf slope are shown in Fig. 6. The simulations are performed using three different speeds of pressure disturbance (22 m/s, 31 m/s and 44 m/s) propagating over this basin from the left (West) to the right (East).

The distributions of water surface (sea states) and sectional views at zero latitude at selected time steps ($t = 10$ min, 20 min, 40 min, 60 min and 90 min) for three different speeds of pressure disturbance moving over the stepwise shelf bathymetry with 1:10 shelf slope are presented in Fig. 7.

Negative and positive amplitudes of the front and rear parts of the generated wave at different time steps for three different speeds of pressure disturbance are given in Table 3.

The simulations for the case of $V = 22$ m/s speed of pressure disturbance (Fig. 7 and Table 2) give a negative wave amplitude changing from −0.188 m to −0.420 m and a positive wave amplitude from 0.268 m to 0.521 m during the 90 min of wave propagation in the basin. In the case of $V = 31$ m/s, the negative amplitude of the wave changes from −0.377 m to −0.621 m and the positive amplitude of the wave changes from 0.453 m to 1.003 m for 90 min of wave propagation in the basin. Furthermore, the obtained values in the case of $V = 44$ m/s show that the negative amplitude of the wave changes from −0.795 m to −0.533 m, and the positive amplitude of the wave changes from 0.832 m to 0.596 m during the 90 min of simulation. However, at around 20 min, the negative amplitude shows the lowest minimum (−1.306 m) as the front of the wave arrives the shelf, and the positive amplitude shows the highest maximum (1.320 m) for $V = 44$ m/s, which

Table 2 Negative and positive amplitudes of the front and rear parts of the wave at different time steps for different slopes (from 200 to 20 m water depths) of the stepwise shelf bathymetry for the case of $V = 31$ m/s speed of pressure disturbance moving over the basin

Time (min)	Amplitude of the depression, front part of the wave							
	1:10	1:100	1:200	1:300	1:400	1:500	1:600	1:700
10	−0.377	−0.377	−0.377	−0.377	−0.377	−0.377	−0.377	−0.377
20	−0.612	−0.397	−0.386	−0.383	−0.382	−0.381	−0.380	−0.380
40	**−0.669**	**−0.742**	−0.696	−0.530	−0.477	−0.451	−0.436	−0.427
60	−0.605	−0.670	**−0.738**	**−0.874**	**−1.052**	**−1.118**	−0.977	−0.739
90	−0.621	−0.694	−0.698	−0.747	−0.743	−0.936	**−1.278**	**−1.463**
110	−0.613	−0.686	−0.696	−0.733	−0.723	−0.770	−0.862	−1.338
*	−0.675	−0.787	−0.794	−0.966	−1.141	−1.292	−1.396	−1.471
Amplitude of the elevation, rear part of the wave								
10	0.453	0.453	0.453	0.453	0.452	0.452	0.453	0.453
20	0.452	0.452	0.452	0.452	0.452	0.452	0.452	0.452
40	0.898	0.774	0.523	0.499	0.470	0.466	0.463	0.462
60	**1.063**	**1.178**	**1.254**	**1.419**	1.289	1.048	0.871	0.780
90	1.003	1.104	1.168	1.396	**1.652**	**1.918**	1.989	2.022
110	0.991	1.096	1.116	1.358	1.588	1.826	**1.990**	**2.079**
*	1.073	1.227	1.354	1.620	1.833	2.016	2.171	2.269

*Extrema of the positive and negative wave amplitudes during the 120 min simulation

Fig. 6 Top and sectional (section A–A) views of the stepwise shelf bathymetry with 1:10 shelf slope
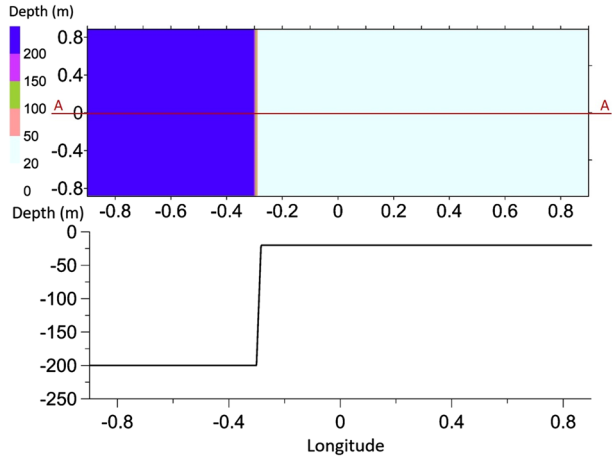
satisfies the Proudman resonance in the deep (left) part of the basin while approaching the shelf slope.

4.2.2 Stepwise shelf bathymetry with 1:700 shelf slope

The top and sectional views of the stepwise shelf bathymetry with 1:700 shelf slope are shown in Fig. 8. The simulations are performed using three different speeds of the pressure disturbance (22 m/s, 31 m/s and 44 m/s) propagating over this basin from the left (West) to the right (East).

The distributions of water surface (sea states) and sectional views at zero latitude at selected time steps ($t = 10$ min, 20 min, 40 min, 60 min and 90 min) for three different speeds of the pressure disturbance, moving over the stepwise shelf bathymetry with 1:700 shelf slope from 200 to 20 m water depths are presented in Fig. 9. The negative and positive amplitudes of the front and rear parts of the generated waves at different time steps for three different speeds of the pressure disturbance are given in Table 4.

It is seen from Fig. 9 and Table 4 that in the case of $V = 22$ m/s speed of pressure disturbance, the negative amplitude of the wave changes from −0.186 m to −0.320 m and the positive amplitude of the wave changes from 0.253 m to 0.281 m during 90 min of the wave propagation in the basin. In the case of $V = 31$ m/s, the negative amplitude of the wave changes from −0.377 m to −1.463 m, and the positive amplitude of the wave changes from 0.453 m to 2.022 m. The results obtained for the case of $V = 44$ m/s also show a negative wave amplitude changing from −0.780 m to −2.385 m and a positive wave amplitude changing from 0.828 m to 3.552 m. In this case, at around 60 min, the negative amplitude shows the lowest minimum (−2.709 m), whereas the positive amplitude shows the highest maximum at around 90 min (3.552 m). In the stepwise shelf bathymetry with a 1:700 slope basin, the maximum wave amplification is observed for the case of $V = 44$ m/s, which satisfies the Proudman resonance in the deep (left) part of the basin while approaching the shelf slope. In other words, the same speeds of pressure disturbance and the wave celerity in the deep (left) part of the basin caused larger amplification of the wave before arriving at the shelf. Furthermore, a higher wave amplification is observed as the wave reaches the top (end) of the
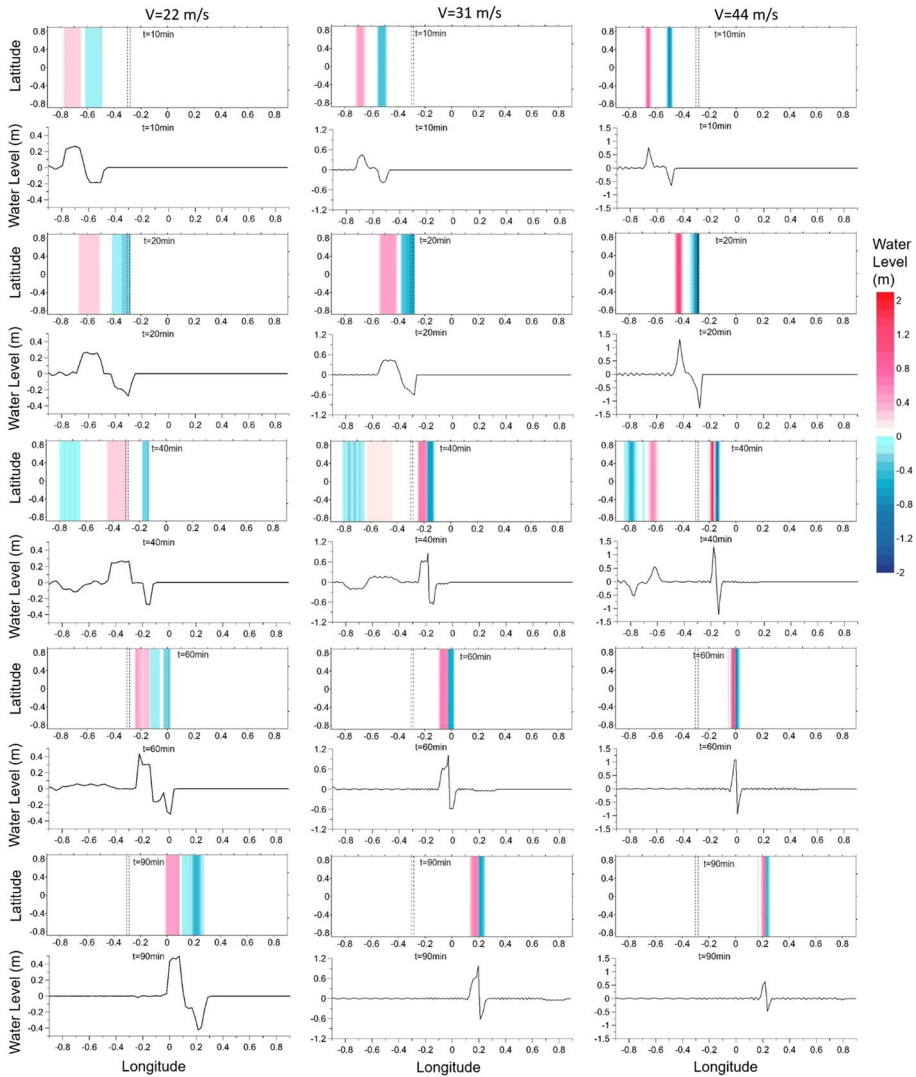
Fig. 7 The sea state at $t = 10$ min, 20 min, 40 min, 60 min, 90 min for the pressure disturbance moving with the speed of 22 m/s (left column), 31 m/s (middle column) and 44 m/s (right column) over the stepwise shelf bathymetry with 1:10 shelf slope. The dashed lines show the sloping section of the basin. Rows 1, 3, 5, 7 and 9 show top view; rows 2, 4, 6, 8 and 10 show sectional views of the water surface at zero latitude (note, vertical scales of sectional views are different). Dashed lines indicate the location of the toe (left) and top (right) of the sloping section of the shelf

sloping section in the East direction. In the stepwise shelf bathymetry with a 1:700 slope basin, the resulting amplitude change is not significant in the case of 22 m/s speed of pressure disturbance.

When we compare the results given in Tables 3 and 4, it is observed that the milder shelf slopes can cause higher wave amplification.

Table 3 Negative and positive amplitudes of the front and rear parts of the wave at different time steps for three different speeds of pressure disturbance moving over the stepwise shelf bathymetry with 1:10 shelf slope from 200 to 20 m water depths

Time (min)	V=22 m/s		V=31 m/s		V=44 m/s	
	Amplitude of the depression, front part of the wave	Amplitude of the elevation, rear part of the wave	Amplitude of the depression, front part of the wave	Amplitude of the elevation, rear part of the wave	Amplitude of the depression, front part of the wave	Amplitude of the elevation, rear part of the wave
10	−0.188	0.268	−0.377	0.453	−0.795	0.832
20	−0.191	0.267	−0.612	0.452	−1.306	1.320
40	−0.232	0.277	−0.669	0.898	−1.217	1.280
60	−0.245	0.301	−0.605	1.063	−0.930	1.070
90	−0.420	0.521	−0.621	1.003	−0.533	0.596

Fig. 8 Top and sectional (section A–A) views of the stepwise shelf bathymetry with 1:700 shelf slope
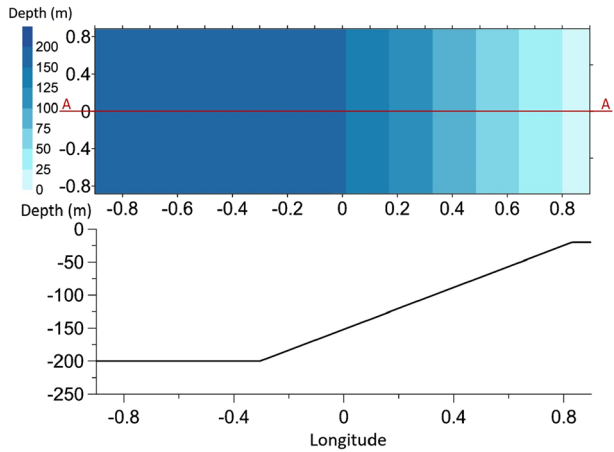
5 Discussions and conclusions

The effects related to the speed of the atmospheric pressure disturbance on the generation and amplification of a meteotsunami in different basins are investigated by using analytical and numerical approaches. In this study, the analytical solution of the wave generation and propagation due to the propagation of the atmospheric pressure disturbance over a flat bottom basin is developed. The numerical model NAMI DANCE solving tsunamis of seismic and landslide origins is upgraded to solving the long-period ocean wave generation and motion due to the spatial and temporal change of the atmospheric pressure and velocity fields. The model is verified by comparing the results with those from analytical solutions on a flat bottom basin. The numerical model is applied to investigate the generation and coastal amplification of the ocean waves in the basins with a triangular lateral cross section and stepwise sloping shelf with different shelf slopes towards shore in the propagation direction.

Analytically, the new solution for meteotsunami generation in the water channel of 'power' cross section (including the channel of triangular cross section) is developed.

For verification of the numerical model NAMI DANCE SUITE, a flat bottom basin, which corresponds to the constant wave celerity (c), is selected. Different speeds of pressure disturbance ($V = 11$ m/s, 22 m/s, 33 m/s, 44 m/s, 55 m/s, 66 m/s) propagating over the 200 m deep flat bottom basin corresponding to different flow conditions (sub-critical, critical and super-critical) are used as the forcing mechanism. Satisfactory agreements between the numerical and analytical results are obtained.

Furthermore, numerical simulations are performed for different water basins: (i) a channel with a triangular cross section, (ii) a stepwise shelf bathymetry with 1:10 shelf slope from 200 to 20 m water depths, and (iii) a stepwise shelf bathymetry with 1:700 shelf slope from 200 to 20 m water depths. For each basin, three different speeds of the pressure disturbance (22 m/s, 31 m/s and 44 m/s) are considered. Additionally, numerical tests for stepwise shelf bathymetry are extended to use different shelf slopes from 1:10 to 1:700.

One of the governing parameters which cause the sea level fluctuations and wave amplification is the relation between the speed of pressure disturbance and the speed of the generated wave in the basin. When the speed of pressure disturbance exceeds the speed of the generated water wave, the generated wave cannot evolve because the
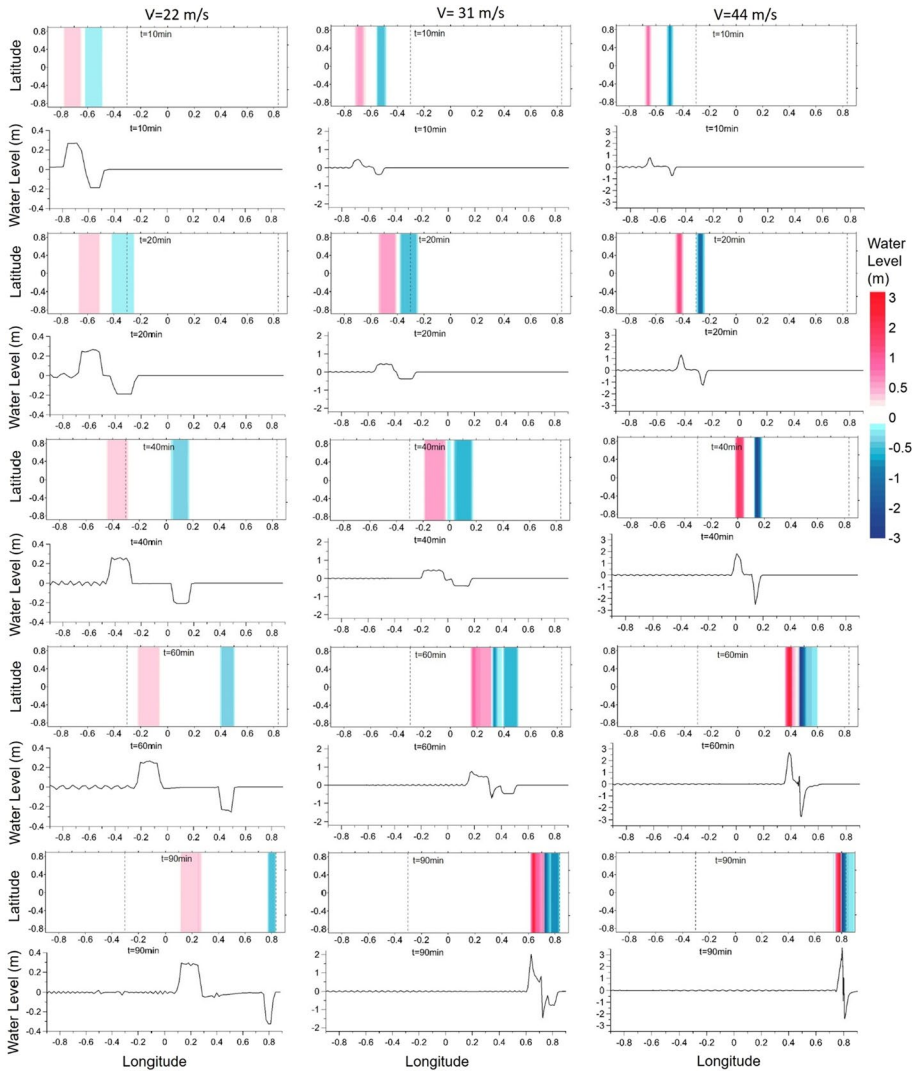
Fig. 9 The sea state at $t = 10$ min, 20 min, 40 min, 60 min, 90 min for $V = 22$ m/s (left column), 31 m/s (middle column) and 44 m/s (right column) over the stepwise shelf bathymetry with 1:700 shelf slope. The dashed lines show the sloping section of the basin. Rows 1, 3, 5, 7 and 9 show top view; rows 2, 4, 6, 8 and 10 show sectional views of the water surface at zero latitude (note, vertical scales of sectional views are different). Dashed lines indicate the location of the toe (left) and top (right) of the sloping section of the shelf

forcing mechanism (pressure disturbance) goes faster and leaves the basin much earlier than the generated wave. On the other hand, when the speed of pressure disturbance is slower than the speed of the generated water wave, the water wave evolves to a certain amplitude (higher amplitudes than in the previous case) and propagates faster than the forcing mechanism (pressure disturbance). Finally, when the pressure disturbance propagates with the same speed of the generated water wave, the wave evolves with the pressure disturbance and propagates with the highest amplitude, as the forcing mechanism

Table 4 The negative and positive amplitudes of the front and rear parts of the wave at different time steps for three different speeds of pressure disturbance over the stepwise shelf bathymetry with 1:700 shelf slope from 200 to 20 m water depths

| Time (min) | $V = 22$ m/s | | $V = 31$ m/s | | $V = 44$ m/s | |
	Amplitude of the depression, front part of the wave	Amplitude of the elevation, rear part of the wave	Amplitude of the depression, front part of the wave	Amplitude of the elevation, rear part of the wave	Amplitude of the depression, front part of the wave	Amplitude of the elevation, rear part of the wave
10	−0.186	0.253	−0.377	0.453	−0.780	0.828
20	−0.186	0.255	−0.380	0.452	−1.342	1.323
40	−0.208	0.251	−0.427	0.462	−2.480	1.825
60	−0.238	0.253	−0.739	0.780	−2.709	2.693
90	−0.320	0.281	−1.463	2.022	−2.385	3.552

propagates together with the generated wave and continuously inputs the energy directly to the generated wave.

Another important factor that leads to the amplification of meteotsunami generated by the propagating pressure disturbance is the bathymetric conditions of the basins. In order to investigate the effects of bathymetric conditions on wave amplification due to the propagating pressure disturbance, different basins with different bathymetric conditions are considered.

Shown for the basin of triangular cross section, the maximum wave amplification is observed at the water depth, where the speed of the pressure disturbance coincides with the wave celerity.

The shelf slope is another parameter affecting the amplification of the wave. Eight different basins of stepwise shelf bathymetry with slopes ranging from 1:10 to 1:700 (sloping section from 200 to 20 m water depth) are used in the simulations. It is shown that for the same speed of the atmospheric pressure disturbance, the amplification over the stepwise shelf bathymetry with milder (1:700) shelf slope is greater than for the steeper (1:10) one, which indicates that the milder shelf slopes can cause higher wave amplification. This is also confirmed with the computed amplitudes for the other slopes (1:100–1:600).

Data availability The data used in this paper are available upon request from the authors.

Compliance with ethical standards

Conflicts of interest The authors declared that they have no conflicts of interest.

References

Airy GB (1878) I. On the tides at Malta. Proceed Royal Soc Lond 26(179–184):485–487
An C, Liu PL, Seo SN (2012) Large-scale edge waves generated by a moving atmospheric pressure. Theor Appl Mech Lett 2(4):042001

Bailey KE, DiVeglio C, Welty A (2014) An examination of the June 2013 East Coast meteotsunami captured by NOAA observing systems. NOAA Technical Report NOS CO-OPS 079. https://repository.library.noaa.gov/view/noaa/14435 (last access on 22.08.2020)

Bechle AJ, Wu CH (2014) The Lake Michigan meteotsunamis of 1954 revisited. Nat Hazards 74(1):155–177

Bubalo M, Janeković I, Orlić M (2018) Chrystal and Proudman resonances simulated with three numerical models. Ocean Dyn 68(4–5):497–507

Bubalo M, Janeković I, Orlić M (2019) Simulation of flooding and drying as an essential element of meteotsunami modelling. Cont Shelf Res 184:81–90

Candella RN (2009) Meteorologically induced strong seiches observed at Arraial do Cabo, RJ, Brazil. Phys Chem Earth Parts A/B/C 34(17–18):989–997

Chen Y, Niu X (2018) Forced wave induced by an atmospheric pressure disturbance moving towards shore. Cont Shelf Res 160:1–9

Cho KH, Choi JY, Park KS, Hyun SK, Oh Y, Park JY (2013) A synoptic study on tsunami-like sea level oscillations along the west coast of Korea using an unstructured-grid ocean model. J Coastal Res 65:678–683

Choi YK, Seo SN (2017) Shock capturing shallow water model for long waves generated by a moving atmospheric pressure. J Coastal Res 79:354–358

Churchill DD, Houston SH, Bond NA (1995) The Daytona Beach wave of 3–4 July 1992: a shallow-water gravity wave forced by a propagating squall line. Bull Am Meteor Soc 76(1):21–32

Denamiel C, Šepić J, Ivanković D, Vilibić I (2019) The Adriatic Sea and Coast modelling suite: evaluation of the meteotsunami forecast component. Ocean Model 135:71–93

Didenkulova I, Pelinovsky E (2012). Resonant generation of tsunami waves by submarine landslides in fjords. Proc. XXII International Offshore and Polar Engineering (ISOPE) Conference, Rhodos Greece, 17–22 June 2012, ISOPE-I-12–393

Didenkulova I, Pelinovsky E (2013) Analytical solutions for tsunami waves generated by submarine landslides in narrow bays and channels. Pure Appl Geophys 170(9–10):1661–1671

Didenkulova I, Nikolkina I, Pelinovsky E, Zahibo N (2010) Tsunami waves generated by submarine landslides of variable volume: analytical solutions for a basin of variable depth. Nat Hazards Earth Syst Sci 10(11):2407–2419

Didenkulova I, Nikolkina I, Pelinovsky E (2011) Resonant amplification of tsunami waves generated by an underwater landslide. Dokl Earth Sci 436(1):66–69

Dogan GG, Annunziato A, Hidayat R, Husrin S, Prasetya G, Kongko W et al. (2021). Numerical simulations of December 22, 2018 Anak Krakatau tsunami and examination of possible submarine landslide scenarios. Pure Appli Geophys, Sulawesi/Palu-2018 and Anak/Krakatau-2018 (ISSN: 0033–4553 (Print) 1420–9136 (Online), 1–20, https://doi.org/10.1007/s00024-020-02641-7.

Donn WL (1959) The Great Lakes storm surge of May 5, 1952. J Geophys Res 64(2):191–198

Dragani WC (2007) Numerical experiments on the generation of long ocean waves in coastal waters of the Buenos Aires province Argentina. Cont Shelf Res 27(5):699–712

Dragani WC, D'Onofrio EE, Grismeyer W, Fiore MM, Campos MI (2009) Atmospherically-induced water oscillations detected in the port of Quequén, Buenos Aires, Argentina. Phys Chem Earth Parts A/B/C 34(17–18):998–1008

Ewing M, Press F, Donn WL (1954) An explanation of the Lake Michigan wave of 26 June 1954. Science 120(3122):684–686

Eze CL, Uko DE, Gobo AET, Sigalo FB, Israel-Cookey C (2009) Mathematical evaluation of tsunami propagation. Res J Appl Sci 4(6):213–216

Garratt JR (1977) Review of drag coefficients over oceans and continents. Mon Weather Rev 105(7):915–929

Greenspan HP (1956) The generation of edge waves by moving pressure distributions. J Fluid Mech 1(06):574–592

Heidarzadeh M, Šepić J, Rabinovich A, Allahyar M, Soltanpour A, Tavakoli F (2020) Meteorological tsunami of 19 March 2017 in the Persian Gulf: observations and analyses. Pure Appl Geophys 177:1231–1259

Hibiya T, Kajiura K (1982) Origin of the Abiki phenomenon (a kind of seiche) in Nagasaki Bay. J Oceanogr Soc Jpn 38(3):172–182

Horvath K, Vilibić I (2014) Atmospheric mesoscale conditions during the Boothbay meteotsunami: a numerical sensitivity study using a high-resolution mesoscale model. In: Vilibić I, Monserrat S, Rabinovich AB (eds) Meteorological tsunamis: The US east coast and other coastal regions. Springer, Cham, pp 55–74

Imamura F (1996) Review of tsunami simulation with a finite difference method. In: Yeh L, Synolakis CE (eds) Long-wave runup models. World Scientific, Singapore

Imamura F, Yalciner A C, Ozyurt G (2006). Tsunami modelling manual. UNESCO IOC international training course on Tsunami Numerical Modelling. http://www.tsunami.civil.tohoku.ac.jp/hokusai3/E/projects/manual-ver-3.1.pdf

Kirby JT, Wei G, Chen Q, Kennedy AB, Dalrymple RA (1998). FUNWAVE 1.0: fully nonlinear Boussinesq wave model-Documentation and user's manual. research report NO. CACR-98–06, University of Delaware

Lipa B, Parikh H, Barrick D, Roarty H, Glenn S (2014) High-frequency radar observations of the June 2013 US East Coast meteotsunami. Nat Hazards 74(1):109–122

Liu PF, Monserrat S, Marcos M, Rabinovich AB (2003a) Coupling between two inlets: observation and modeling. J Geophys Res Oceans 108(C3):3069

Liu PLF, Lynett P, Synolakis CE (2003b) Analytical solutions for forced long waves on a sloping beach. J Fluid Mech 478:101–109

Lynett PJ, Gately K, Wilson R, Montoya L, Arcas D, Aytore B et al (2017) Inter-model analysis of tsunami-induced coastal currents. Ocean Model 114:14–32

Melinand B (2015) A mathematical study of meteo and landslide tsunamis: the Proudman resonance. Nonlinearity 28(11):4037–4080

Mercer D, Sheng J, Greatbatch RJ, Bobanović J (2002) Barotropic waves generated by storms moving rapidly over shallow water. J Geophys Res Oceans 107(C10):16–21

Metin AD (2016). Long waves generation and coastal amplification due to atmospheric pressure disturbances. (Master's thesis), Middle East Technical University. Retrieved from http://etd.lib.metu.edu.tr/upload/12620257/index.pdf

Monserrat S, Ibbetson A, Thorpe AJ (1991) Atmospheric gravity waves and the 'rissaga' phenomenon. Q J R Meteorol Soc 117(499):553–570

Monserrat S, Vilibić I, Rabinovich AB (2006) Meteotsunamis: atmospherically induced destructive ocean waves in the tsunami frequency band. Nat Hazards Earth Syst Sci 6(6):1035–1051

Niu X, Chen Y (2020) Energy accumulation during the growth of forced wave induced by a moving atmospheric pressure disturbance. Coast Eng J 62(1):23–34

Niu X, Zhou H (2015) Wave pattern induced by a moving atmospheric pressure disturbance. Appl Ocean Res 52:37–42

Orlić M, Belušić D, Janeković I, Pasarić M (2010) Fresh evidence relating the great Adriatic surge of 21 June 1978 to mesoscale atmospheric forcing. J Geophys Res Oceans. https://doi.org/10.1029/2009JC005777

Papadopoulos GA (1993) On some exceptional seismic (?) sea-waves in the Greek archipelago. Sci Tsunami Hazards 11:25–34

Park YH (1986) Water characteristics and movements of the Yellow Sea Warm Current in summer. Prog Oceanogr 17(3):243–254

Pasquet S, Vilibić I (2013) Shelf edge reflection of atmospherically generated long ocean waves along the central US East Coast. Cont Shelf Res 66:1–8

Pattiaratchi CB, Wijeratne EMS (2015) Are meteotsunamis an underrated hazard? Philos Trans Royal Soc A Math Phys Eng Sci 373(2053):20140377

Paxton CH, Sobien DA (1998) Resonant interaction between an atmospheric gravity wave and shallow water wave along Florida's west coast. Bull Am Meteor Soc 79(12):2727–2732

Pelinovsky E (2006) Hydrodynamics of tsunami waves. In: Grue J, Trulsen K (eds) Waves in geophysical fluids cism international centre for mechanical sciences. Springer, Vienna

Powell MD, Vickery PJ, Reinhold TA (2003) Reduced drag coefficient for high wind speeds in tropical cyclones. Nature 422(6929):279–283

Proudman J (1929) The effects on the sea of changes in atmospheric pressure. Geophys Supp Monthly Notices Royal Astron Soc 2(4):197–209

Rabinovich AB (2009) Seiches and harbor oscillations. Handb Coast Ocean Eng. https://doi.org/10.1142/9789812819307_0009

Rabinovich AB (2020) Twenty-seven years of progress in the science of meteorological tsunamis following the 1992 Daytona Beach event. Pure Appl Geophys 177:1193–1230

Rabinovich AB, Monserrat S (1996) Meteorological tsunamis near the balearic and kuril islands: descriptive and statistical analysis. Nat Hazards 13(1):55–90

Rabinovich AB, Monserrat S, Fain IV (1999) Numerical modeling of extreme seiche oscillations in the region of the Balearic Islands. Oceanology 39(1):16–24

Romero R, Vich M, Ramis C (2019) A pragmatic approach for the numerical prediction of meteotsunamis in Ciutadella harbour (Balearic Islands). Ocean Model 142:101441. https://doi.org/10.1016/j.ocemod.2019.101441

Sallenger AH Jr, List JH, Gelfenbaum G, Stumpf RP, Hansen M (1995) Large wave at Daytona Beach, Florida, explained as a squall-line surge. J Coastal Res 11(4):1383–1388

Šepić J, Vilibić I, Strelec Mahović N (2012) Northern Adriatic meteorological tsunamis: Observations, link to the atmosphere, and predictability. J Geophys Res Oceans. https://doi.org/10.1029/2011JC007608

Šepić J, Vilibić I, Fine I (2015) Northern Adriatic meteorological tsunamis: assessment of their potential through ocean modeling experiments. J Geophys Res Oceans 120(4):2993–3010

Šepić J, Rabinovich AB, Sytov VN (2018) Odessa Tsunami of 27 June 2014: observations and numerical modelling. Pure Appl Geophys 175:1545–1572

Sozdinler CO, Yalciner AC, Zaytsev A (2015) Investigation of tsunami hydrodynamic parameters in inundation zones with different structural layouts. Pure Appl Geophys 172(3):931–952

Tanaka K (2010) Atmospheric pressure-wave bands around a cold front resulted in a meteotsunami in the East China Sea in February 2009. Nat Hazards Earth Syst Sci 10(12):2599–2610

Thiebaut S, Vennell R (2011) Resonance of long waves generated by storms obliquely crossing shelf topography in a rotating ocean. J Fluid Mech 682:261–288

Tinti S, Bortolucci E (2000) Analytical investigation of tsunamis generated by submarine slides. Ann Geofis 43:519–536

Tinti S, Bortolucci E, Chiavettieri C (2001) Tsunami excitation by submarine slides in shallow-water approximation. Pure Appl Geophys 158(4):759–797

Titov VV, Synolakis CE (1998) Numerical modeling of tidal wave run-up. J Waterway Port Coast Ocean Eng 124(4):157–171

Velioglu Sogut D, Yalciner AC (2019) Performance comparison of NAMI DANCE and FLOW-3D® models in tsunami propagation, inundation and currents using NTHMP benchmark problems. Pure Appl Geophys 176:3115–3153

Vennell R (2007) Long barotropic waves generated by a storm crossing topography. J Phys Oceanogr 37(12):2809–2823

Vennell R (2010) Resonance and trapping of topographic transient ocean waves gener ated by a moving atmospheric disturbance. J Fluid Mech 650:427–442

Vilibić I (2008) Numerical simulations of the Proudman resonance. Cont Shelf Res 28(4–5):574–581

Vilibić I, Domijan N, Orlić M, Leder N, Pasarić M (2004) Resonant coupling of a traveling air pressure disturbance with the east Adriatic coastal waters. J Geophys Res Oceans. https://doi.org/10.1029/2004JC002279

Vilibić I, Monserrat S, Rabinovich A, Mihanović H (2008) Numerical modelling of the destructive meteotsunami of 15 June, 2006 on the coast of the Balearic Islands. Pure Appl Geophys 165(11):2169–2195

Vilibić I, Šepić J, Ranguelov B, Mahović NS, Tinti S (2010) Possible atmospheric origin of the 7 May 2007 western Black Sea shelf tsunami event. J Geophys Res Oceans. https://doi.org/10.1029/2009JC005904

Vučetić T, Vilibić I, Tinti S, Maramai A (2009) The great adriatic flood of 21 June 1978 revisited: an overview of the reports. Phys Chem Earth Parts A/B/C 34(17–18):894–903

Wang X, Li K, Yu Z, Wu J (1987) Statistical characteristics of seiches in Longkou Harbour. J Phys Oceanogr 17(7):1063–1065

Watts P, Grilli ST, Kirby JT, Fryer GJ, Tappin DR (2003) Landslide tsunami case studies using a Boussinesq model and a fully nonlinear tsunami generation model. Nat Hazards Earth Syst Sci 3(5):391–402

Yalciner AC, Pelinovsky E (2007) A short cut numerical method for determination of resonance periods of free oscillations in irregular shaped basins. Ocean Eng 34(5–6):747–757

Yalciner B, Zaytsev A. (2017) Assessment of efficiency and performance of tsunami numerical modeling with GPU. Abstract EGU2017–1246 Presented in European Geoscience Union, EGU April 2017, https://meetingorganizer.copernicus.org/EGU2017/EGU2017-1246.pdf

Yalciner AC, Kian R, Aytore B, Zaytsev A (2015) Harbors and tsunami threat; a case study in the Sea of Marmara. In Proceedings of 36th IAHR World Congress, 4pages, Delft, Netherland, 28 June–3 July, 2015

Yalciner B, Zaytsev A, Yalciner AC (2017) Accelerated solutions in tsunami simulation and visualization with case studies. Abstract presented in the 28th International Tsunami Symposium. 21–25 August 2017, Bali Indonesia

Publisher's Note Springer Nature remains neutral with regard to jurisdictional claims in published maps and institutional affiliations.

Authors and Affiliations

Gozde Guney Dogan[1] · Efim Pelinovsky[2,3] · Andrey Zaytsev[4] · Ayse Duha Metin[1] · Gulizar Ozyurt Tarakcioglu[1] · Ahmet Cevdet Yalciner[1] ⑩ · Bora Yalciner[1,5] · Ira Didenkulova[6,7,8]

✉ Ahmet Cevdet Yalciner
yalciner@metu.edu.tr

[1] Department of Civil Engineering, Ocean Engineering Research Center, Middle East Technical University, Ankara, Turkey

[2] Sector of Extreme Wave Phenomena, Institute of Applied Physics, Nizhny Novgorod, Russia

[3] Higher School of Economics, National Research University, Nizhny Novgorod, Russia

[4] Special Research Bureau for Automation of Marine Researches, Far Eastern Branch of Russian Academy of Sciences, Yuzhno-Sakhalinsk, Russia

[5] Department of Computer Engineering, Middle East Technical University, Ankara, Turkey

[6] Nizhny Novgorod State Technical University N.a. R.E. Alekseev, Nizhny Novgorod, Russia

[7] Department of Marine Systems, Tallinn University of Technology, Tallinn, Estonia

[8] Department of Mathematics, University of Oslo, Oslo, Norway